RSC Advances

PAPER

View Article Online
View Journal | View Issue

Cite this: *RSC Adv.*, 2023, **13**, 33430

A novel yttrium stabilized zirconia and ceria composite electrolyte lowering solid oxide fuel cells working temperature to 400 °C†

Yu Liu,[a] Liwen Zuo,[a] Yulian Ye,[a] Cong Jiang,[a] Dan Zheng,[b] Chunlei Liu,*[a] Baoyuan Wang *[ab] and Xunying Wang *[ab]

Received 7th March 2023
Accepted 6th September 2023

DOI: 10.1039/d3ra01507f

rsc.li/rsc-advances

Reducing the working temperature and improving the ionic conductivity of electrolytes have been the critical challenges for the gradual development of solid oxide fuel cells (SOFCs) in practical applications. The researchers all over the world attempt to develop alternative electrolyte materials with sufficient ionic conductivity. In this work, YSZ–CeO_2 composite material was used as electrolytes in the construction of symmetrical SOFCs. The maximum power densities (P_{max}) of YSZ–CeO_2 based fuel cell can reach 680 mW cm^{-2} at 450 °C, 510 mW cm^{-2} at 430 °C, 330 mW cm^{-2} at 410 °C and even 200 mW cm^{-2} as the operational temperature was reduced to 390 °C. A series of characterizations indicates that the activation energy of the YSZ–CeO_2 composite is significantly decreased, and the enhancement effect for ion conduction comes from interface transport. Our findings indicate the YSZ–CeO_2 composite material can be a highly promising candidate for advanced low-temperature SOFC.

1 Introduction

Energy is the basic driving force of world development, and is also one of the three major substances for human survival in modern society. Unfortunately, the non-renewable nature of fossil energy and the excessive exploitation, use and waste of fossil energy have brought it to the brink of exhaustion. Besides, the excessive exploitation also caused serious environmental problems. Therefore, renewable energy must be developed to realize the sustainable development of human society.[1–3] Solid oxide fuel cells (SOFCs) can directly convert chemical energy into electricity. Compared with traditional energy conversion systems, SOFCs, as a clean energy conversion technology, have high energy conversion efficiency[4–6] and fuel flexibility. However, high working temperature (800–1000 °C) is the key technical problem for SOFCs, which greatly limits the commercial development.[7,8] Therefore, reducing the working temperature of SOFCs meanwhile maintaining high performance of fuel cells has been the research direction that researchers are interested in.

In previous studies, various ionic conductors such as yttrium stabilized zirconia (YSZ), gadolinium doped cerium (GDC) and $La_{1-x}Sr_xGa_{1-y}Mg_yO_{3-\delta}$ (LSGM) have been widely used as electrolytes for SOFCs.[9–11] Among them, YSZ is considered as the most successful electrolyte material so far, but its poor ionic conductivity at low temperature limits its application in low temperature SOFC (LT-SOFC).[12,13] One common way to increase the low temperature performance of SOFC with YSZ based electrolyte is to decrease the thickness of the electrolyte layer.[14] However, due to the thickness of thin-film electrolyte has to be restricted by the requirement of gas densification and mechanical strength for the electrolyte layer, the SOFC with YSZ thin-film electrolyte is still hard to work at temperature lower than 500 °C.[15–17] Recently, it has been discovered that hetero-interfaces can provide fast ionic conduction route, and constructing hetero-structure is an effective way to increase the ionic conductivity.[18,19]

Ceria (CeO_2) has been shown to be multifunctional in many fields, such as lithium batteries, fuel cells and a series of energy-related devices, which has attracted extensive interest from researchers.[20,21] The most important feature of CeO_2 is the capacity for storing and releasing oxygen through Ce^{4+}/Ce^{3+} redox cycles, which largely depends on the type and concentration of oxygen vacancies in the lattice and surface structure. Unique physical properties are associated with Ce^{3+} ions and oxygen vacancies.[22] According to relevant researches, the formed $CeO_{2-\delta}$@CeO_2 core–shell heterostructure may contributes to the development of electrolytes with high ionic conductivity under low temperature, and the hypoxic layer on the surface provides fast ion transport pathways.[23,24]

On the basis of these ideas, in our work, a novel YSZ–CeO_2 composite material is fabricated from nitrate ($Ce(NO_3)_3$)-yttrium stabilized zirconia (YSZ) composite and was adopted as

[a]School of Microelectronics, Hubei University, Wuhan, Hubei, 430062, PR China. E-mail: wangxunying@hubu.edu.cn; baoyuanw@163.com; liuchunlei7788945@163.com

[b]Hubei Yangtze Memory Laboratories, Wuhan, 430205, China

† Electronic supplementary information (ESI) available. See DOI: https://doi.org/10.1039/d3ra01507f

electrolyte in the symmetric fuel cell assembled with Ni-NCAL ($Ni_{0.8}Co_{0.15}Al_{0.05}LiO_{2-\delta}$) as the electrodes. Study results revealed that the fabricated fuel cell possesses excellent output power densities at around 400 °C. Various characterizations have been used to systematically study the characteristics of YSZ–CeO_2 composite material, and the results validate the great potential application value of YSZ–CeO_2 composite electrolytes in LT-SOFCs.

2 Experimental

2.1 Materials fabrication

In our study, the cerium nitrate hexahydrate ($Ce(NO_3)_3 \cdot 6H_2O$) with purity ≥99.5% was purchased from Macklin company. YSZ powder was directly purchased from Inframat company. The YSZ–CeO_2 composite material was prepared using the following procedure. Firstly, $Ce(NO_3)_3 \cdot 6H_2O$ powder was mixed with 8YSZ (8 mol% Y_2O_3) powder together. The mixture was thoroughly blended after being ground for 2 hours, and then placed in muffle furnace to calcine at 600 °C for 3 hours. Finally, the homogeneous YSZ–CeO_2 composite powder materials with different mass ratios (50 : 50, 60 : 40, 70 : 30, 80 : 20 and 85 : 15) were obtained after being fully ground.

2.2 Physical characterizations

X-ray diffractometer (Bruker AXS D8 Advance) was used to obtain X-ray diffraction (XRD) patterns. Field emission scanning electron microscopy (FESEM, JSM7100F) equipped with Oxford energy-dispersive spectrometer (EDS) was used to examine the surface morphology and element distribution of samples. The detailed morphology at interface region between two phases was further investigated by high revolution transmission electron microscopy (HR-TEM, JEOL JE-2100F). The valence states of the elements were examined by X-ray photoelectron spectroscopy (XPS, Escalab 250Xi, Thermo Fisher Scientific). Raman analysis of the material was conducted on Renishao *via* China with wavelength of 532 nm. To detect the electrical conductivity, YSZ–CeO_2 powder was compressed under a pressure of 500 MPa to obtain pellets with diameter of 13 mm, followed by being brushed Pt paste for ionic conductivity test or Ag paste for electronic conductivity test. Linear scan voltage (LSV) method was adopted to characterize the conductivity of the materials, which was conducted on digital source instrument (Keithley 2460).

2.3 SOFC fabrication and electrochemical characterization

The symmetrical electrode pieces were fabricated as follows: NCAL slurry was prepared by mixing commercial NCAL powder with turpentine permeable alcohol in a mass ratio of 3 : 1, and then the slurry was painted evenly with a brush on the nickel foam, finally dried the NCAL coated nickel foam at 110 °C for 7–10 minutes to finish the preparation of NCAL electrode pieces. Wherein the nickel foam acts as current collector and gas diffusion layer, while NCAL is responsible for catalytical reaction. The YSZ–CeO_2 composite powder was sandwiched by two pieces of Ni–NCAL to construct Ni–NCAL/YSZ–CeO_2/Ni–NCAL configuration, which was pressed under a loading of 500 MPa for 1–2 minutes to complete fuel cell fabrication. Before the electrochemical performance testing, the cell was pre-treated by H_2 at 450 °C for 30 minutes. During the test, hydrogen was supplied as the fuel and ambient air served as the oxidant. The current density–voltage (*I–V*) and current density–power (*I–P*) curves of the assembled cells were recorded by electronic load (IT8511, ITECH). The electrochemical impedance spectroscopy (EIS) was characterized by Gamry Reference 3000 electrochemical workstation in open-circuit voltage mode, with an AC signal amplitude of 10 mV and frequency range of 0.1–10^6 Hz.

3 Results and discussion

Fig. 1(a) presented the SEM images of the as-prepared YSZ–CeO_2 (70 : 30) powder. Obviously, the particle size of YSZ–CeO_2 composite material was in nanometer level with irregular shape. Fig. 1(b) showed the XRD pattern of the original YSZ–CeO_2 material. The diffraction peaks located at 30.1°, 34.9°, 50.1°, 59.6°, 62.5°, 73.6°, 81.6° and 84.1° can be indexed to (1 0 1), (0 0 2), (1 1 2), (1 0 3), (2 0 2), (0 0 4), (2 1 3) and (1 1 4) planes of fluorite YSZ (JCPDS No. 82-1244), respectively; these peaks at 28.7°, 33.2°, 47.7°, 56.6°, 69.7°, 77.1°, 79.5° and 88.9° are corresponded to the (1 1 1), (2 0 0), (2 2 0), (3 1 1), (4 0 0), (3 3 1), (4 2 0), (4 2 2) planes of fluorite cubic phase of CeO_2 (JCPDS No. 75-0076), respectively. There are no other stray peaks in the pattern, indicating that there is no impurity in the YSZ–CeO_2 (70 : 30) composite. Fig. 1(c) displays the typical Raman spectrum of the hydrogen treated YSZ–CeO_2 (70 : 30) material. The strong Raman peak centered at about 465 cm^{-1} is corresponding to the F_{2g} symmetric stretching mode of the Ce–8O vibrational unit.[25–27] The weak peak located at about 260 cm^{-1} is assigned to the second-order mode of CeO_2.[28] And the Raman peaks at approximately 623 cm^{-1} and 150 cm^{-1} are indexed to YSZ.[29] This indicates that the chemical state of the YSZ–CeO_2 (70 : 30) material under H_2 atmosphere is stable.

To assess the potential of YSZ–CeO_2 composite electrolyte for SOFC, typical current density–voltage (*I–V*) and current–power density (*I–P*) curves of Ni–NCAL/YSZ–CeO_2/Ni–NCAL fuel cells with different compositions of YSZ to CeO_2 were tested using H_2 as fuel and air as oxidant at 550 °C. Obviously, as Fig. 2(a) depicts, the composition of YSZ–CeO_2 electrolyte significantly influences the electrochemical performance of assembled cell. The peak power density (P_{max}) initially enhanced with the increase of CeO_2 content, and then decreased as the CeO_2 content further increased. The P_{max} of 760 mW cm^{-2} and open-circuit voltages (OCV) of 1.08 V were obtained for the fuel cell with YSZ–CeO_2 (70 : 30, wt/wt) composite electrolyte. Fig. 2(b) further gives the electrochemical performance of the SOFC with the YSZ-CeO_2 (70 : 30, wt/wt) composite at various temperatures. It was discovered that the fuel cell delivered exciting electrochemical performance in low temperature range, 680 mW cm^{-2}, 510 mW cm^{-2}, and 330 mW cm^{-2} at 450 °C, 430 °C and 410 °C, respectively, and can even maintain at 200 mW cm^{-2} as the operational temperature reduced to 390 °C. The P_{max} of this fuel cell device under 390–450 °C is much higher than those reported in the ref. 30–32.

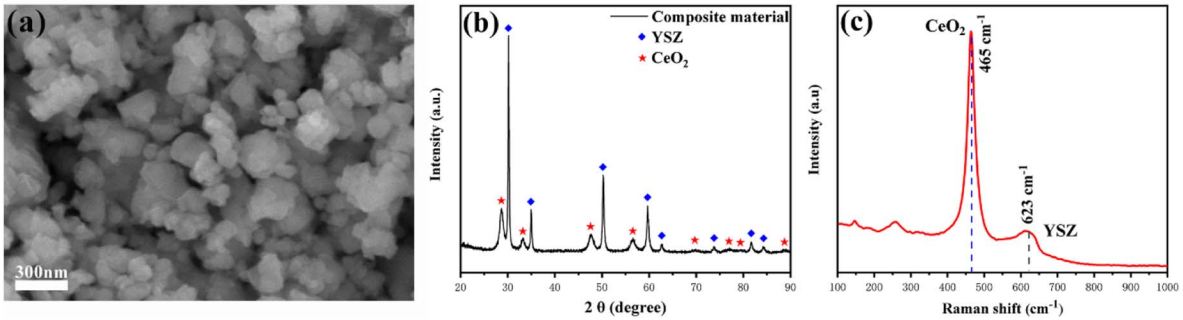

Fig. 1 (a) The SEM images of the as-prepared YSZ–CeO_2 (70 : 30) powders, (b) the XRD patterns of YSZ–CeO_2 (70 : 30) and (c) Raman spectrum of hydrogen treated YSZ–CeO_2 (70 : 30) powder.

The unexpected cell performance at low temperature indicated that the YSZ–CeO_2 composite developed in this work has enormous advantage in electrolyte application for low temperature SOFC. To further study the reason for excellent performance of the YSZ–CeO_2 composite at low temperature, the corresponding EIS for the fuel cell working at 450 °C was conducted and analyzed. Besides, for comparison, the EIS of the SOFC with YSZ electrolyte was also tested under the same conditions. The tested spectra were shown in Fig. 2(c), and the inset presented the equivalent circuit of $R_0(R_1Q_1)(R_2Q_2)$ for simulation. Table 1 lists the corresponding fitting results. Q represents constant phase element (CPE) which describe the

Table 1 The EIS fitting results

T (450 °C)	R_0	Q_1	n_1	R_1	Q_2	n_2	R_2
YSZ–CeO_2	0.1958	0.3733	0.5211	0.1044	2.4040	0.7347	0.1903
YSZ	0.6648	0.1283	0.4438	0.3193	0.9026	0.6764	0.6729

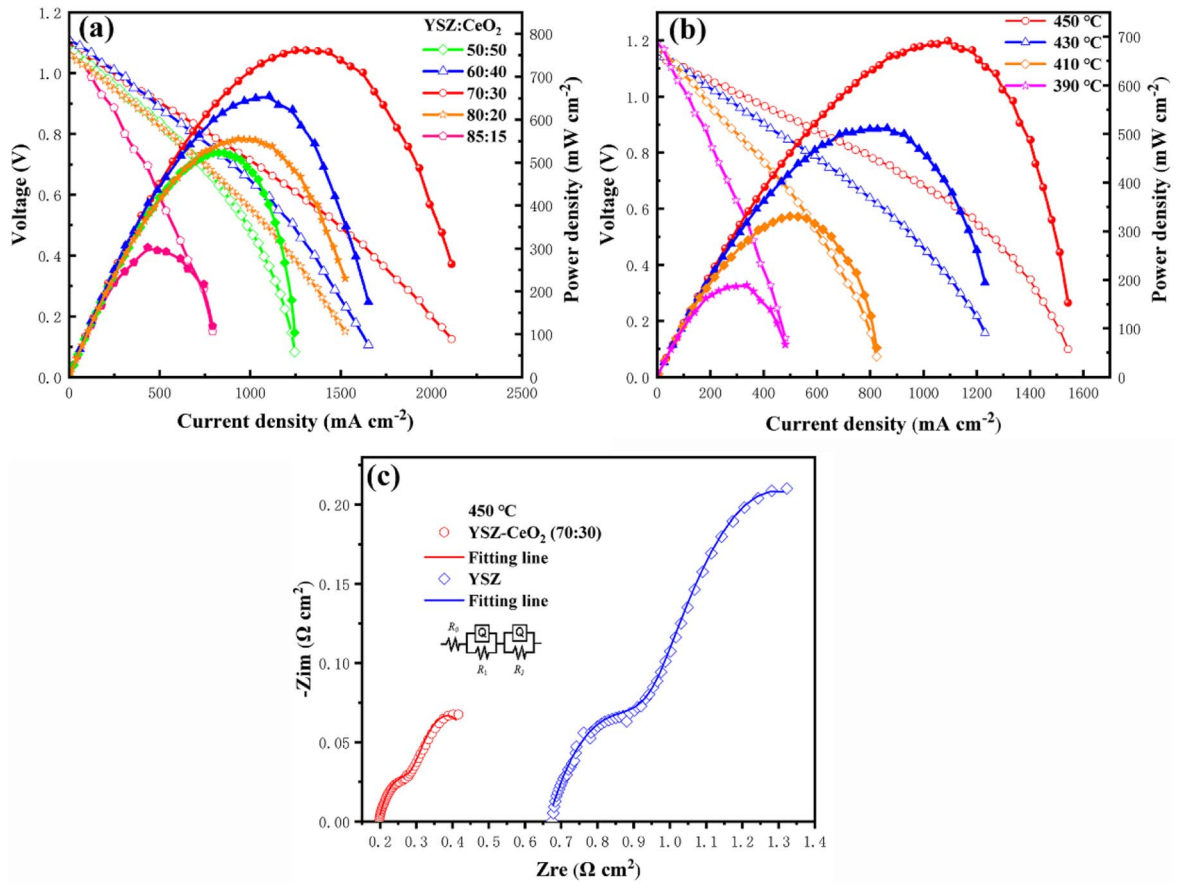

Fig. 2 (a) I–V and I–P characteristics of fuel cells based on YSZ–CeO_2 electrolyte with different composition operated at 550 °C; (b) electrochemical performance of YSZ–CeO_2 (70 : 30, wt/wt) based SOFC measured at 450 °C–390 °C; (c) EIS curves of SOFC with YSZ–CeO_2 (70 : 30, wt/wt) electrolyte and SOFC with YSZ electrolyte under 450 °C (dots for experimental data; line for fitting data). H_2 and air were adopted as fuel and oxidant, respectively.

electric double layer at the interface between electrode and electrolyte.[33,34] R_0 reveals the high frequency intercept on the real axis and represents the ohmic resistance, which includes the bulk ionic conduction resistance of the electrolyte, the electronic conduction resistance of the electrodes, and the contact resistance associated with the interface between electrodes and electrolyte layer. R_1 corresponds to the first arc at the intermediate frequency and is designated as the grain boundary ionic conduction resistance.[35] R_2 represents the low-frequency arc and belongs to the charge transfer process.[36] It can be seen that both R_0 and R_1 of the SOFC with YSZ–CeO_2 (70 : 30, wt/wt) composite electrolyte are lower than those of the SOFC with YSZ electrolyte. The electrodes of the two fuel cells are the same, therefore it indicates that the YSZ–CeO_2 composite possesses both lower bulk ionic conduction resistance and lower grain boundary ionic conduction resistance. Moreover, lower R_2 of the YSZ–CeO_2 based fuel cell indicates it also possesses lower charge transfer resistance. Based on the above discussions, the excellent ionic conductivity of the composite electrolyte leads to more tri-phase interfaces at the interface between electrodes and electrolyte layer, which is beneficial to improve the catalyst utilization, and thus decreases the charge transfer resistance. Moreover, it is well known that Ce^{4+} in CeO_2 can be reduced to Ce^{3+} by H_2 in the SOFC working environment, which can increase the electrolyte electronic conductivity.[37] Therefore, the stability of the Ce element in the YSZ–CeO_2 (70 : 30, wt/wt) composite electrolyte was characterized by XPS (Fig. S1†). As shown in Fig. S1,† the ratio of Ce^{3+}/Ce^{4+} in the original electrolyte is about 3 : 7, while it increased to about 4 : 6 for the electrolyte which had experienced fuel cell test. Thus the electron conductivity of the H_2 treated electrolyte was further investigated (Fig. S2†). The calculated results showed that the electron conductivity of the H_2 treated electrolyte was too low, and thus the effect of electronic leakage of the electrolyte layer on the SOFC performance can be ignored.

Fig. 3(a) gives the cross-sectional SEM image of the fuel cell using the YSZ–CeO_2 (70 : 30, wt/wt) electrolyte after performance testing in H_2/Air at 450 °C. It clearly shows a dense and uniform morphology without stratification, which indicates the well matching of thermal expansion coefficient between electrodes and electrolyte. The EDS mappings of cell obtained from cross-sectional SEM image are shown in Fig. 3(b)–(h). Ni, Co and O elements can be obviously detected on both electrode sides, which identified the composition of the electrode. Besides, due to the content of Al element in NCAL electrode is too small (1.3%), the it is hard to distinguish the distribution of Al in electrodes and electrolyte layer. The atomic mass of Li is too light to be detected by EDS detector. Elements such as Ce, Y, Zr and O can be observed in the electrolyte layer. Moreover, the uniform distribution of these elements in the electrolyte layer indicates that the two-phase materials are mixed evenly, which is conducive to the establishment of continuous and uniform ion conduction network. And a high-magnification image of the electrolyte layer in Fig. 3(k) shows that YSZ–CeO_2 composite layer is dense and no through-holes, which is beneficial to prevent gas leakage. The detailed morphology of cathode and anode are showed in Fig. 3(i) and (j), respectively. The porous nature of the NCAL electrode makes it easier for air or H_2 to diffuse through the electrodes. In addition, after performance testing the anode exhibited significantly different morphology compared with cathode. The NCAL on cathode side presented as micrometer sphere, whereas the NCAL material in anode side is small particles. It is due to that the NCAL in the anode are reduced by H_2, and thus the sphere appearance changed.[38]

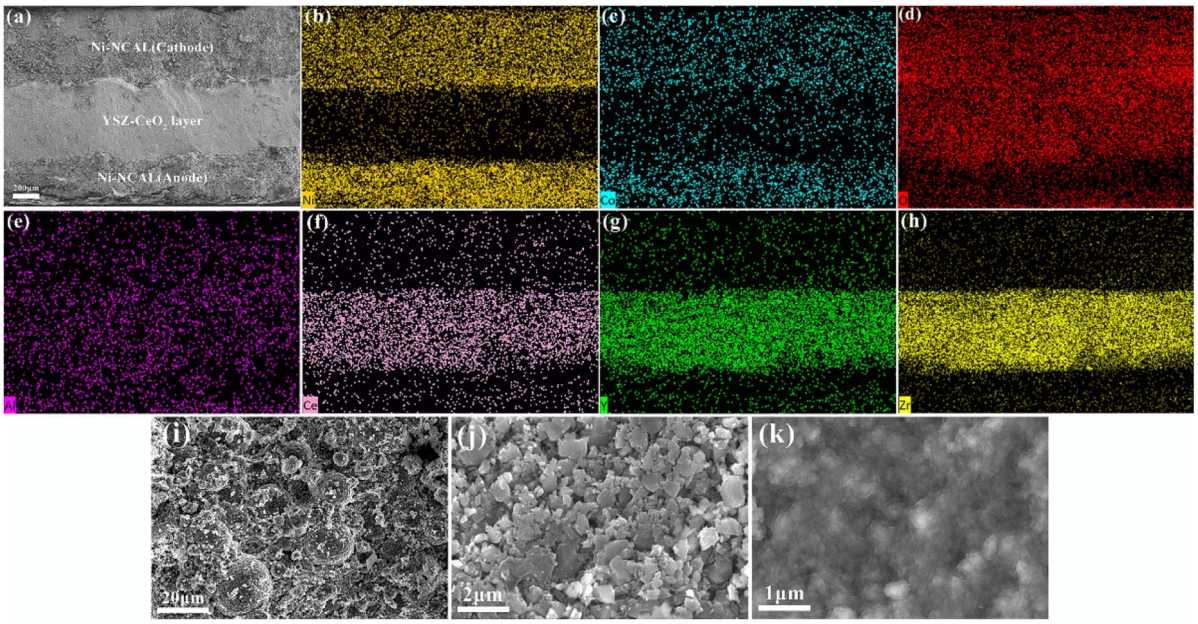

Fig. 3 (a) Cross-sectional SEM images of the tested fuel cell with YSZ–CeO_2 (70 : 30, wt/wt) electrolyte, (b)–(h) EDS mappings of the tested fuel cell from the cross-sectional view, magnified SEM images of (i) cathode region, (j) anode region, and (k) detailed morphology of the YSZ–CeO_2 (70 : 30, wt/wt) electrolyte membrane.

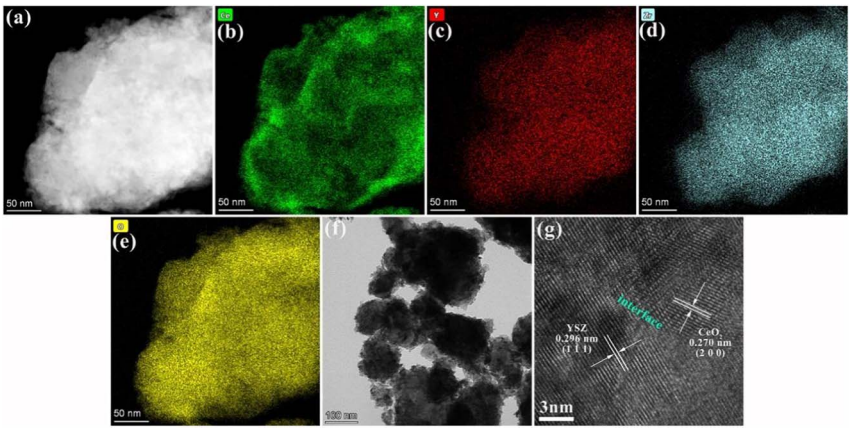

Fig. 4 (a) TEM and corresponding EDS images of (b) Ce, (c) Y, (d) Zr and (e) O elements, (f and g) HR-TEM images of the tested YSZ–CeO_2 electrolyte.

To investigate the detailed information of the YSZ–CeO_2 composite morphology and phase distribution, the YSZ–CeO_2 (70 : 30, wt/wt) composite was further observed by HR-TEM. Fig. 4(b)–(e) depict the associated TEM-EDS mapping images. The agglomeration of Ce element in the edge indicates the YSZ–CeO_2 composite material is core–shell structure with YSZ as core and CeO_2 as shell. As depicted in Fig. 4(f), the TEM image enlarged at low magnification shows that the particle size distribution of YSZ–CeO_2 composite materials ranges from tens to hundreds of nanometers. The corresponding HR-TEM image is shown in Fig. 4(g). The lattice fringes at 0.296 nm and 0.270 nm correspond to the (1 1 1) plane of YSZ and the (2 0 0) plane of CeO_2, respectively. The relative unordered elemental distribution in the interface between YSZ and CeO_2 is beneficial to provide fast ion conduction path, and thus improve the ionic conductivity of the material.[39,40] This also explains the reason for the lower ionic conduction resistance of the YSZ–CeO_2 composite compared with YSZ electrolyte (Fig. 2(c)).

The conductivities of the original YSZ–CeO_2 (70 : 30, wt/wt) electrolyte were further characterized in different environments. The charge carriers are different in different environments. Electrons are the main charge carriers when the SOFC device is in N_2 environment; O^{2-} and electrons are the main charge carriers when the SOFC device is in air environment; H^+ and electrons are the main charge carriers when the SOFC device is in H_2 environment. The proton conductivities obtained in hydrogen atmosphere as a function of temperature were expressed in Fig. 5(a). The activation energy of proton motion of the original YSZ–CeO_2 electrolyte is found to be 0.47 eV at 400–500 °C according to the Arrhenius curve, which is much lower than those of reported for YSZ (1.16 eV at 300 °C–600 °C).[41–43] The activation energy is the average difference between the energies of activated molecules and ordinary molecules. The much lower activation energy indicating that within this temperature range, the energy needed for proton transport from its normal state to an active state is relatively low, thus proton transport is easier for the YSZ–CeO_2 electrolyte than YSZ. Fig. 5(b) gives the Arrhenius curve of the tested YSZ–CeO_2 electrolyte obtained in air atmosphere, it can be inferred

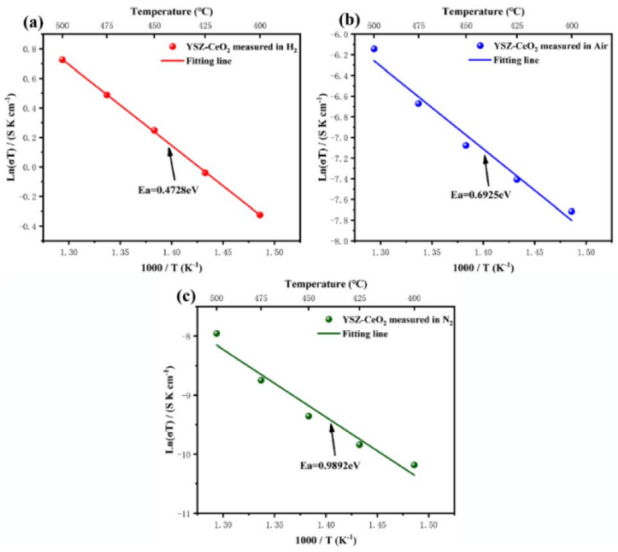

Fig. 5 Arrhenius curves of the original YSZ–CeO_2 electrolyte obtained in different atmospheres: (a) H_2, (b) air and (c) N_2.

that the activation energy of the composite material under air atmosphere is 0.69 eV, which is higher than that under H_2 atmosphere. Moreover, it can be seen that the conductivity of electrolyte in H_2 is much higher than in air. Namely the conductivity of the YSZ–CeO_2 electrolyte membrane was mainly attributed by proton conduction, which facilitates the outstanding low temperature performance due to the easier transportation of proton than O^{2-}.[44,45] As shown in Fig. 5(c), the electronic conductivity obtained in N_2 environment is relatively low in the 400–500 °C temperature range, which is favorable for cell performance.

XPS characterizations were used to analyze the chemical state of oxygen element in YSZ–CeO_2 (70 : 30, wt/wt) electrolyte before and after performance test. The spectra are decomposed into several peaks that are assigned to different symmetric signals.[46] Lattice oxygen (O_L) in YSZ or CeO_2 is belong to the peak centered at about 529 eV, while the higher binding energy

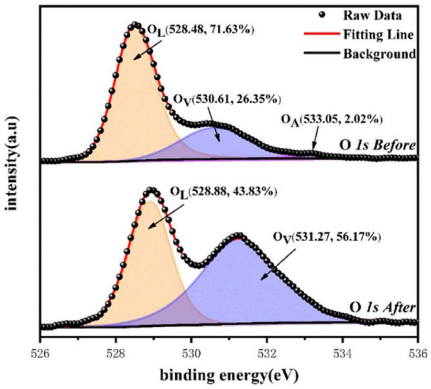

Fig. 6 XPS curves for O 1s of the original and tested YSZ–CeO_2 (70 : 30, wt/wt) electrolyte.

peak at about 531 eV is attributed to the oxygen atoms in the deficiency regions (O_V).[47] As can be seen in Fig. 6, after the performance test of fuel cells, the area ratio of O_V increases from 26.35% to 56.17%, thus it can be inferred that more oxygen vacancies were generated *in situ* in the electrolyte during fuel cell operation. This may be due to the reduction of Ce^{4+} to Ce^{3+} during the fuel cell operation. The increase of oxygen vacancy content is beneficial to increase the ionic conductivity of the fuel cell under low temperature, which is also one reason for the excellent low temperature performance of the SOFC.

4 Conclusions

The output power of the SOFC with YSZ–CeO_2 (70 : 30, wt/wt) composite electrolyte at 450 °C can reach 680 mW cm^{-2}. Evenly, the P_{max} can maintain at 200 mW cm^{-2} as the operational temperature reduced to 390 °C. The excellent performance indicates that the YSZ–CeO_2 composite electrolyte can still work normally at around 400 °C. The enhanced ionic conductivity of the YSZ–CeO_2 composite electrolyte compared with YSZ electrolyte provides the basis for higher cell performance. Moreover, the activation energy of proton movement in YSZ–CeO_2 composite electrolyte is lower than that of oxygen ion movement, indicating that the composite electrolyte is a kind of proton conduction material, which is more suited to working under low temperature. The hetero-interface formed in the composite helped to improve ionic conductivity. These study results demonstrate the high potential of the YSZ–CeO_2 composite electrolyte in low-temperature SOFCs.

Conflicts of interest

There are no conflicts to declare.

Acknowledgements

The authors would like to acknowledge the financial support from the National Natural Science Foundation of China (Grant No. 51872080), Wuhan Science and Technology Bureau (No. 2020010601012293).

Notes and references

1 B. Zhu, P. D. Lund, R. Raza, Y. Ma, L. Fan, M. Afzal, J. Patakangas, Y. He, Y. Zhao, W. Tan, Q.-A. Huang, J. Zhang and H. Wang, *Adv. Energy Mater.*, 2015, **5**, 1401895.
2 C. Xia, Z. Qiao, C. Feng, J. S. Kim, B. Wang and B. Zhu, *Materials*, 2017, **11**, 40.
3 C. Xia, Z. Qiao, L. Shen, X. Liu, Y. Cai, Y. Xu, J. Qiao and H. Wang, *Int. J. Hydrogen Energy*, 2018, **43**, 12825–12834.
4 A. Gilane, S. Fop, F. Sher, R. I. Smith and A. C. McLaughlin, *J. Mater. Chem. A*, 2020, **8**, 16506–16514.
5 C. Xia, Y. Mi, B. Wang, B. Lin, G. Chen and B. Zhu, *Nat. Commun.*, 2019, **10**, 1707.
6 X. Liu, W. Dong, Y. Tong, L. Wei, M. Yuan, X. Wang, B. Wang and B. Zhu, *Electrochim. Acta*, 2019, **295**, 325–332.
7 Z. Gao, L. V. Mogni, E. C. Miller, J. G. Railsback and S. A. Barnett, *Energy Environ. Sci.*, 2016, **9**, 1602–1644.
8 A. Rafique, R. Raza, N. Akram, M. Kaleem Ullah, A. Ali, M. Irshad, K. Siraj, M. A. Khan, B. Zhu and R. Dawson, *RSC Adv.*, 2015, **5**, 86322–86329.
9 B. Yadian, R. Chen, H. Liu, H. Sun, Q. Liu, C. L. Gan, Z. Kun, C. Zhao, B. Zhu and Y. Huang, *Nano Res.*, 2015, **8**, 1857–1864.
10 W. Lee, S.-Y. Chen, Y.-S. Chen, C.-L. Dong, H.-J. Lin, C.-T. Chen and A. Gloter, *J. Phys. Chem. C*, 2014, **118**, 26359–26367.
11 Y. Cai, C. Xia, B. Wang, W. Zhang, Y. Wang and B. Zhu, *ACS Sustain. Chem. Eng.*, 2017, **5**, 10387–10395.
12 S. Fop, K. S. McCombie, E. J. Wildman, J. M. S. Skakle, J. T. S. Irvine, P. A. Connor, C. Savaniu, C. Ritter and A. C. McLaughlin, *Nat. Mater.*, 2020, **19**, 752–757.
13 W. Dong, Y. Tong, B. Zhu, H. Xiao, L. Wei, C. Huang, B. Wang, X. Wang, J.-S. Kim and H. Wang, *J. Mater. Chem. A*, 2019, **7**, 16728–16734.
14 Z. Qiao, C. Xia, Y. Cai, M. Afzal, H. Wang, J. Qiao and B. Zhu, *J. Power Sources*, 2018, **392**, 33–40.
15 B. Wang, Y. Wang, L. Fan, Y. Cai, C. Xia, Y. Liu, R. Raza, P. A. van Aken, H. Wang and B. zhu, *J. Mater. Chem. A*, 2016, **4**, 15426–15436.
16 Y. Lin, R. Ran and Z. Shao, *Int. J. Hydrogen Energy*, 2010, **35**, 8281–8288.
17 A. D. Liyanage, S. D. Perera, K. Tan, Y. Chabal and K. J. Balkus, *ACS Catal.*, 2014, **4**, 577–584.
18 H. You, C. Zhao, B. Qu, G. Guan and A. Abudula, *J. Alloys Compd.*, 2016, **669**, 46–54.
19 T. Hong, K. S. Brinkman and C. Xia, *ChemElectroChem*, 2016, **3**, 805–813.
20 S. Sengodan, R. Lan, J. Humphreys, D. Du, W. Xu, H. Wang and S. Tao, *Renewable Sustainable Energy Rev.*, 2018, **82**, 761–780.
21 H. Li, A. Petz, H. Yan, J. C. Nie and S. Kunsági-Máté, *J. Phys. Chem. C*, 2011, **115**, 1480–1483.
22 B. Xu, Q. Zhang, S. Yuan, S. Liu, M. Zhang and T. Ohno, *Catal. Today*, 2017, **281**, 135–143.
23 Y. Xing, Y. Wu, L. Li, Q. Shi, J. Shi, S. Yun, M. Akbar, B. Wang, J.-S. Kim and B. Zhu, *ACS Energy Lett.*, 2019, **4**, 2601–2607.
24 B. Wang, B. Zhu, S. Yun, W. Zhang, C. Xia, M. Afzal, Y. Cai, Y. Liu, Y. Wang and H. Wang, *NPG Asia Mater.*, 2019, **11**, 15.

25 M. Valášková, J. Kupková, G. S. Martynková, J. Seidlerová, V. Tomášek, M. Ritz, K. Kočí, V. Klemm and D. Rafaja, *Appl. Clay Sci.*, 2018, **151**, 164–174.
26 F. Meng, L. Wang and J. Cui, *J. Alloys Compd.*, 2013, **556**, 102–108.
27 Z. Wu, M. Li, J. Howe, H. M. Meyer 3rd and S. H. Overbury, *Langmuir*, 2010, **26**, 16595–16606.
28 F. Liang, Y. Yu, W. Zhou, X. Xu and Z. Zhu, *J. Mater. Chem. A*, 2015, **3**, 634–640.
29 T. Li, M. Zhang, Y. Yuan, S. Muhammad, H. Nishijima and W. Pan, *Solid State Ionics*, 2018, **326**, 11–17.
30 F. He, S. Liu, T. Wu, M. Yang, W. Li, G. Yang, F. Zhu, H. Zhang, K. Pei, Y. Chen, W. Zhou and Z. Shao, *Adv. Funct. Mater.*, 2022, **32**, 2206756.
31 M. Liang, Y. Song, D. Liu, L. Xu, M. Xu, G. Yang, W. Wang, W. Zhou, R. Ran and Z. Shao, *Appl. Catal., B*, 2022, **318**, 121868.
32 C. Duan, J. Tong, M. Shang, S. Nikodemski, M. Sanders, S. Ricote, A. Almansoori and R. O'Hayre, *Science*, 2015, **349**, 1321–1326.
33 Z. He, J. Nie, K. Liu, K. Sivajee Ganesh, M. Akbar, C. Xia, X. Wang, W. Dong, J. Huang and B. Wang, *Int. J. Hydrogen Energy*, 2021, **46**, 9799–9808.
34 L. Fan, H. Zhang, M. Chen, C. Wang, H. Wang, M. Singh and B. Zhu, *Int. J. Hydrogen Energy*, 2013, **38**, 11398–11405.
35 H. Hu, Q. Lin, Z. Zhu, X. Liu, M. Afzal, Y. He and B. Zhu, *J. Power Sources*, 2015, **275**, 476–482.
36 H. Hu, Q. Lin, A. Muhammad and B. Zhu, *J. Power Sources*, 2015, **286**, 388–393.
37 P. Vinchhi, M. Khandla, K. Chaudhary and R. Pati, *Inorg. Chem. Commun.*, 2023, **152**, 110724.
38 Y. Meng, W. Zhang, Z. He, C. Liu, J. Gao, M. Akbar, R. Guo, S. Zhou, Y. Ji, X. Wang and Y. Yang, *Int. J. Hydrogen Energy*, 2021, **46**, 9874–9881.
39 A. Gayen, K. R. Priolkar, P. R. Sarode, V. Jayaram and S. Emura, *Chem. Mater.*, 2004, **16**, 2317–2328.
40 S. S. Liu, S. Toh, T. Daio, M. Koyama and S. Matsumura, *ECS Trans.*, 2013, **57**, 1401–1405.
41 O. O. Agbede, K. Hellgardt and G. H. Kelsall, *Mater. Today Chem.*, 2020, **16**, 100252.
42 O. Kwon and G. Choi, *Solid State Ionics*, 2006, **177**, 3057–3062.
43 C.-C. T. Yang, W.-C. J. Wei and A. Roosen, *Mater. Chem. Phys.*, 2003, **81**, 134–142.
44 T. Shimonosono, Y. Hirata, Y. Ehira, S. Sameshima, T. Horita and H. Yokokawa, *Solid State Ionics*, 2004, **174**, 27–33.
45 S. J. Litzelman and H. L. Tuller, *Solid State Ionics*, 2009, **180**, 1190–1197.
46 R. C. Rabelo-Neto, H. B. E. Sales, C. V. M. Inocêncio, E. Varga, A. Oszko, A. Erdohelyi, F. B. Noronha and L. V. Mattos, *Appl. Catal., B*, 2018, **221**, 349–361.
47 E. Paparazzo, *J. Phys.: Condens.Matter*, 2018, **30**, 343003.